Theoretical calculation of the laser characteristics of a transversely excited CO_2 laser

1991 J. Phys. D: Appl. Phys. 24 1258

(http://iopscience.iop.org/0022-3727/24/8/006)

J. Phys. D: Appl. Phys. 24 (1991) 1258–1269. Printed in the UK

Theoretical calculation of the laser characteristics of a transversely excited CO_2 laser

Kaung-Hsiung Wu† and Ching-Sheng Lie‡

† Department of Electrophysics, ‡ Institute of Electro-Optical Engineering, National Chiao Tung University, 30050 Hsinchu, Taiwan, Republic of China

Received 18 February 1991

Abstract. This paper presents a theoretical model of a transversely excited cw CO_2 laser. The laser rate equations, as well as the basic hydrodynamic and thermodynamic equations, have been used to describe the whole laser system. The spatial distributions of small signal gain and saturation intensity along the gas flow direction have been calculated for a given set of initial conditions, namely, pumping rate, gas mixture, total pressure, gas temperature and gas flow velocity. The dependence of laser output power on discharge and flow parameters is in good agreement with the experimental data, confirming the usefulness of this model and understanding of the laser performance.

1. Introduction

Continuous wave output, transversely excited (CW TE) convectively cooled, CO_2 lasers have been used widely for industrial applications. In order to achieve the optimum performances of the laser behaviour, a theoretical analysis of this kind of CO_2 laser is of considerable significance.

The development of the theoretical model of TE CO_2 lasers followed the simulation of gas dynamic CO_2 lasers which were reported by Cool [1], Tulip and Seguin [2], Morse *et al* [3] and Anderson [4]. Several papers have developed CW TE CO_2 laser models for their specific systems. For example, the work of Yoder *et al* [5] was concerned with electron beam sustained lasers and the work of Armandillo and Kaye [6] was concerned with transverse flow lasers in which the current distribution was obtained from empirical data. The model presented here is similar to the work of Cool [1]. However, in that work, all the electrical excitation was assumed to occur upstream of the optical cavity so that only relaxation effects occurred in the cavity itself; and it also assumed that gas density, pressure, temperature and gas flow velocity are constant along the gas flow direction. The spatial variations of small signal gain and saturation intensity along the gas flow direction could be solved by a coupled set of differential equations, but it was very complex and tedious. In this paper the pumping rate has been added in the kinetic equations and the spatial distribution of electron density along the gas flow direction, which was obtained from the empirical data, is taken into account. Moreover, the spatial variations of the gas parameters such as gas temperature, pressure, density and flow velocity along the flow direction are also considered in this theoretical model. In order to simplify the numerical process, the optical cavity along the gas flow direction is divided into many thin layers, as shown in figure 1. In each layer, the gas kinetic and thermodynamic equations with known boundary conditions are solved. We can then obtain the average quantities of laser parameters such as population density, small signal gain, saturation intensity, and output power and gas parameters within this region. The new values of the working parameters and boundary conditions at the exit of this small region can also be obtained from these equations and will be the initial conditions for the next layer. The procedure will be repeated sequentially in each thin slab region throughout the discharge region. Therefore, the spatial distributions of laser and gas parameters along the gas flow direction can be

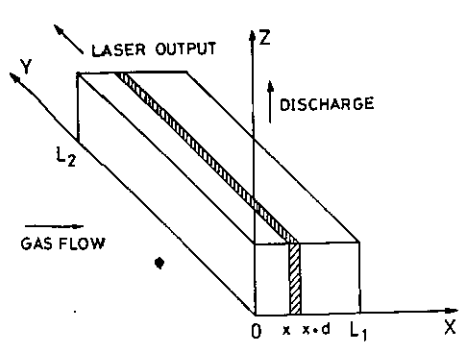

Figure 1. A TE laser in which gas flow, discharge current and optical axis are mutually perpendicular.

0022-3727/91/081258 + 12 $03.50

achieved under different discharge and gas conditions. This represents an attempt to use the simplest possible method to solve this problem. A PASCAL program generates numerical solutions to give good agreement with the experimental results and thus provides a useful tool for understanding and optimizing this type of laser.

In section 2 the theoretical model of the TE CW CO_2 lasers is described. The laser kinetic and thermodynamic equations are formulated. The calculation of small signal gain, saturation intensity, laser output power and gas parameters are also presented. In section 3, the computational and numerical processes are described. The experimental apparatus is introduced briefly and the discharge current distribution for the laser system has been formulated. The computational procedure and numerical flow chart are also explained in detail in this section. The numerical results are shown and discussed in section 4. These results are also compared with the experimental data. In the appendix, the analytical solutions of small signal gain and saturation intensity within a small region are presented.

2. Theoretical model

2.1. Assumptions

Figure 1 shows the schematic diagram of a TE CO_2 laser system in which the gas flow, discharge current, and optical axis are perpendicular to each other. The equations to describe this system can be derived under the following assumptions [6–9].

(a) Each vibrational mode has a Boltzmann distribution characterized by its own temperature.

(b) Energy transfer between rotational and translational mode is very rapid. Thus the rotational and translational state of the gas mixture can be represented by the kinetic gas temperature.

(c) The symmetric and the bending modes of CO_2 are closely coupled by the fast Fermi resonance, and can be characterized by a common temperature.

(d) Stimulated emission occurs only for P(20) transitions in the $(0\,0^0 1, J) \rightarrow (1\,0^0 0, J+1)$ band.

(e) The gas transport through the discharge region is in the positive x direction and it is assumed to be an inviscid constant area flow.

(f) The diffusion process can be neglected for the high-speed flow lasers.

(g) Spatial distribution of the glow discharge and gas flow are uniform along both the optical axis (y axis) and the discharge axis (z axis). Thus the electric field, current density, gas flow velocity, pressure, and temperature all depend explicitly only on the flow direction.

(h) Since both SnO_2-coated devices and monolithic catalysts have been introduced in the laser system, the dissociation rate of CO_2 can be neglected [10].

(i) A steady state condition is considered in each thin layer.

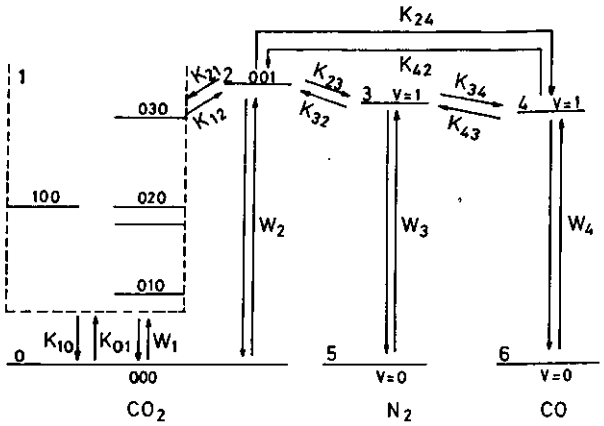

Figure 2. Energy level diagram of vibrational levels of CO_2, N_2 and CO.

2.1. Kinetic rate equations

For a CO_2:CO:N_2:He laser system, the main vibrational energy levels of the electronic ground states for the CO_2, N_2 and CO molecules are illustrated in figure 2. There are seven groups of levels defined. Group 0 is the single ground state level $(00^0 0)$; group 1 is a combination of closely coupled states consisting of the bending vibrational state $(02^0 0)$, $(02^2 0)$, $(01'0)$, and the symmetric stretch state $(10^0 0)$; group 2 is the upper laser level $(00^0 1)$; group 3 is the N_2 vibrational modes ($v = 1$ to $v = 8$); group 4 is the CO vibrational modes ($v = 1$ to $v = 8$); group 5 is the N_2 ground state ($v = 0$) and group 6 is the CO ground state. Of the numerous energy transfer processes which occur in this laser system, the processes shown in figure 2 are found to be the most important and will be considered in the model. The discharge region along the gas flow direction is separated into many thin layers. Consider one of the layers which is located between x and $x + d$ in the flow direction. The steady state rate equations can be written as [1]:

$$u\frac{\partial N_1'}{\partial x} = W_1' - k_{10}N_1' + k_{21}N_2' - k_{12}N_1' + (B_{21}N_2' - B_{12}N_1')g(\nu)\frac{J'}{ch\nu} \tag{1a}$$

$$u\frac{\partial N_2'}{\partial x} = W_2' - k_{21}N_2' + k_{12}N_1' - (B_{21}N_2' - B_{12}N_1')g(\nu)\frac{J'}{ch\nu} + k_{32}N_3' - k_{23}N_2' + k_{42}N_4' - k_{24}N_2' \tag{1b}$$

$$u\frac{\partial N_3'}{\partial x} = W_3' - k_{32}N_3' + k_{23}N_2' + k_{43}N_4' - k_{34}N_3' \tag{1c}$$

$$u\frac{\partial N_4'}{\partial x} = W_4' - k_{43}N_4' + k_{34}N_3' - k_{42}N_4' + k_{24}N_2' \tag{1d}$$

$$\frac{\partial J'}{\partial y} = h\nu(B_{21}N_2' - B_{12}N_1')g(\nu)\frac{J'}{ch\nu} \tag{1e}$$

$$N_0' + N_1' + N_2' = N_{CO_2} \tag{1f}$$

$$N_3' + N_5' = N_{N_2} \tag{1g}$$

$$N_4' + N_6' = N_{CO} \tag{1h}$$

where N_i' is the ith group population density (cm^{-3}) at the local position, W_i' is the electron excitation for the ith group particles, k_{ij} is the collision rate between groups i and j, $g(\nu)$ is the line shape function, B_{ij} is the Einstein B coefficient between i and j, J' is the laser intensity (erg s^{-1} cm^{-2}), N_{CO_2}, N_{N_2}, N_{CO} are total number density of CO_2, N_2 and CO molecules respectively (cm^{-3}) and u is the uniform flow velocity in the small region.

Define

$$N_i = \frac{1}{d}\int_x^{x+d} N_i'\,dx$$

$$J = \frac{1}{d}\int_x^{x+d} J'\,dx$$

and

$$W_i = \frac{1}{d}\int_x^{x+d} W_i'\,dx$$

as the average quantities within the small interval between x and $x+d$. Integrating both parts of equations (1), assuming uniform conditions in the y direction, gives

$$\frac{u}{d}(N_{1,x+d}' - N_{1,x}') = W_1 - k_{10}N_1 + k_{21}N_2 - k_{12}N_1 + (B_{21}N_2 - B_{12}N_1)\frac{J}{ch\nu} \tag{2a}$$

$$\frac{u}{d}(N_{2,x+d}' - N_{2,x}') = W_2 - k_{21}N_2 + k_{12}N_1 - (B_{21}N_2 - B_{12}N_1)\frac{J}{ch\nu} + k_{32}N_3 - k_{23}N_2 + k_{42}N_4 - k_{24}N_2 \tag{2b}$$

$$\frac{u}{d}(N_{3,x+d}' - N_{3,x}') = W_3 - k_{32}N_3 + k_{23}N_2 + k_{43}N_4 - k_{34}N_3 \tag{2c}$$

$$\frac{u}{d}(N_{4,x+d}' - N_{4,x}') = W_4 - k_{43}N_4 + k_{34}N_3 - k_{42}N_4 + k_{24}N_2 \tag{2d}$$

$$\frac{\partial J}{\partial y} = h\nu(B_{21}N_2 - B_{12}N_1)g(\nu)\frac{J}{ch\nu} \tag{2e}$$

where $N_{i,x}'$ and $N_{i,x+d}'$ are the population density of the ith group at position x and $x+d$, respectively. Equations (2a)–(2e) are five equations in nine unknowns. Another four equations should be added to solve these unknowns. For the case of $J=0$, another four equations can be obtained:

$$W_1 - k_{10}N_1^0 - k_{12}N_1^0 + k_{21}N_2^0 - k_f(N_{1,x+d}'^0 - N_{1,x}'^0) = 0 \tag{3a}$$

$$W_2 - k_{21}N_2^0 + k_{12}N_2^0 + k_{32}N_3^0 - k_{23}N_2^0 + k_{42}N_4^0 - k_{24}N_2^0 - k_f(N_{2,x+d}'^0 - N_{2,x}'^0) = 0 \tag{3b}$$

$$W_3 - k_{32}N_3^0 + k_{23}N_2^0 + k_{43}N_4^0 - k_{34}N_3^0 - k_f(N_{3,x+d}'^0 - N_{3,x}'^0) = 0 \tag{3c}$$

$$W_4 - k_{43}N_4^0 + k_{34}N_3^0 - k_{42}N_4^0 + k_{24}N_2^0 - k_f(N_{4,x+d}'^0 - N_{4,x}'^0) = 0 \tag{3d}$$

where the superscripts 0 represent N_i for the $J=0$ case.

From equations (2) with the initial conditions $N_{i,x}'^0$ ($i=1,2,3,4$) at the position x, we can solve $N_{i,x+d}'^0$ by using the Runge–Kutta method.

Comparing equations (2) and (3), gives the following conditions:

$$N_i + N_{i,x}' - N_{i,x+d}' = N_i^0 + N_{i,x}'^0 - N_{i,x+d}'^0 \qquad (i=1,2,3,4). \tag{4}$$

Then, from equations (2) and (4), we obtain the following equations:

$$A_1 - (k_{10} + k_f + k_{12})N_1 + k_{21}N_2 + (B_{21}N_2 - B_{12}N_1)g(\nu)\frac{J}{ch\nu} + k_fN_1^0 = 0 \tag{5a}$$

$$A_2 + k_{12}N_1 - (k_{21} + k_{23} + k_{24} + k_f)N_2 - (B_{21}N_2 - B_{12}N_1)g(\nu)\frac{J}{ch\nu} + k_{32}N_3 + k_{42}N_4 + k_fN_2^0 = 0 \tag{5b}$$

$$A_3 + k_{23}N_2 - (k_{32} + k_{34} + k_f)N_3 + k_{43}N_4 + k_fN_3^0 = 0 \tag{5c}$$

$$A_4 + k_{24}N_2 + k_{34}N_3 - (k_{42} + k_{43} + k_f)N_4 + k_fN_4^0 = 0 \tag{5d}$$

$$\frac{dJ}{dy} = h\nu(B_{21}N_2 - B_{12}N_1)g(\nu)\frac{J}{ch\nu} = g_{th}J \tag{5e}$$

where $A_i = W_i + k_f(N_{i,x}^0 - N_{i,x+d}^0)$, $k_f = u/d$, and g_{th} is the threshold gain which is equal to the loss for steady state condition.

Solving equations (3) and (5) simultaneously, we obtain $N_i^0(x)$, $N_i(x)$, and $J(x)$. The numerical procedure will be shown in the next section. In the appendix the analytical solutions are also presented.

2.3. Hydrodynamic and thermodynamic equations

In order to derive the ambient gas temperature T, the hydrodynamic and thermodynamic equations for the

gas transport through the discharge region should be considered. These equations can be described by the one-dimensional (1D) conservation equations written in differential form as follows [6].

(a) Gas flow continuity equation

$$\frac{1}{\rho}\frac{\mathrm{d}\rho}{\mathrm{d}x}+\frac{1}{u}\frac{\mathrm{d}u}{\mathrm{d}x}=0 \tag{6}$$

where ρ is the gas density.

(b) Conservation of momentum

$$\frac{\mathrm{d}p}{\mathrm{d}x}+\rho u\frac{\mathrm{d}u}{\mathrm{d}x}=0 \tag{7}$$

where p is gas pressure.

(c) Conservation of energy

$$\rho u\frac{\mathrm{d}h}{\mathrm{d}x}-u\frac{\mathrm{d}p}{\mathrm{d}x}=I_c(x)E(x)-e_{\text{laser}} \tag{8}$$

where h is the enthalpy per unit mass, $I_c(x)$ is the current density in the discharge, $E(x)$ is the electric field in the discharge. e_{laser} is the laser output power per unit volume:

$$=\frac{1}{c}\int_0^{\nu}(B_{21}N_2-B_{12}N_1)g(\nu)J\,\mathrm{d}\nu.$$

(d) Equation of an ideal gas

$$p=\rho RT \tag{9}$$

The gas enthalpy may be written as

$$h=C_pT+\sum_{i=1}^{4}\frac{\varepsilon_iN_i}{\rho_i} \tag{10}$$

where C_p is the specific heat under constant pressure and ε_i is the vibrational energy for the ith group particles.

The changes of gas parameters can be written as

$$\frac{\Delta\rho}{\rho}=-\frac{\Delta u}{u} \tag{11}$$

$$\frac{\Delta p}{p}=\frac{\Delta T}{T}\left(1-\frac{RT}{u^2}\right)^{-1}=\frac{\Delta\rho}{\rho}+\frac{\Delta T}{T} \tag{12}$$

$$\Delta T=\frac{1}{\rho u}\left(I_cE-e_{\text{laser}}-u\frac{\mathrm{d}}{\mathrm{d}x}\sum_i\varepsilon_iN_{i,x}\right)\times\left(C_p-\frac{R}{1-(RT/u^2)}\right)^{-1}. \tag{13}$$

If the initial values of gas temperature, pressure, velocity, and density at x are known, then from equations (11) to (13), we can obtain new gas parameters at the boundary $x+d$ as

$$T_{x+d}=T_x+\Delta T\cdot d \tag{14a}$$

$$p_{x+d}=p_x+\Delta p\cdot d \tag{14b}$$

$$u_{x+d}=u_x+\Delta u\cdot d \tag{14c}$$

$$\rho_{x+d}=p_x+\Delta\rho\cdot d. \tag{14d}$$

2.4. Small signal gain, saturation intensity and laser output power

The unsaturated gain g_0 is expressed as

$$g_0=\frac{1}{c}(B_{21}N_2^0-B_{12}N_1^0)g(\nu) \tag{15}$$

where $g(\nu)$ is the line shape function which depends on the broadening mechanism and is chosen as a Lorentzian line shape for a high-pressure (~100 Torr) laser system [11]. A Lorentzian line shape with the centre frequency ν_0 and the width at half maximum $\Delta\nu$ is given by

$$g(\nu_0)=\lim_{\nu\to\nu_0}\frac{\Delta\nu}{2\pi}\frac{1}{(\nu-\nu_0)^2+(\Delta\nu/2)^2}=\frac{2}{\pi\Delta\nu} \tag{16}$$

where [9]

$$\Delta\nu=\sum_t\frac{N_tQ_t}{\pi}\left[\frac{8kT}{\pi}\left(\frac{1}{M_{CO_2}}+\frac{1}{M_t}\right)\right]^{1/2} \tag{17}$$

and M_t and Q_t are the mass and collision section area of molecule t, respectively.

The small signal gain at centre frequency can then be written as:

$$g_0=\frac{c^2}{8\pi h\nu_0^3}\frac{2}{\pi\Delta\nu}\Delta N^0 \tag{18}$$

where

$$\Delta N^0=N_2^0P(J_R)-N_1^0\frac{2J_R+3}{2J_R+1}P(J_R+1) \tag{19}$$

$$P(J_R)=\frac{2h_cBr}{kT}(2J_R+1)\exp\left(\frac{-hcBrJ_R(J_R+1)}{kT}\right) \tag{20}$$

and Br is the rotational coefficient.

For the case of homogenous broadening, the gain coefficient $g(\nu,J)$ can be expressed as

$$g(\nu,J)=\frac{g_0}{1+J/J_s} \tag{21}$$

where J_s is the saturation intensity.

Solving equations (5), the analytical solution (see appendix) of J_s is

$$J_s=ch\nu\left(\frac{B_{12}}{k_{10}+k_f}+\frac{B_{21}(k_{32}+k_f)(k_{42}+k_f)}{(k_{21}+k_f)(k_{32}+k_f)(k_{42}+k_f)+k_{23}k_f(k_{42}+k_f)+k_{24}k_f(k_{32}+k_f)}\right)^{-1}. \tag{22}$$

It is noteworthy that the saturation intensity depends on the relaxation time of the energy levels, stimulated emission cross sections, and the gas flow velocity.

The growth of laser intensity along the optical axis can be written as:

$$\frac{dJ}{dy} = h\nu(B_{21}N_2 - B_{12}N_1)g(\nu)\frac{J}{ch\nu} = g_{th}J \quad (23)$$

and the boundary conditions are as follows. At $y = 0$

$$J_0^+ = R_1 J_0^- \qquad R_1 = 1 - a_1 - t_1 \quad (24)$$

and at $y = L_2$

$$J_{L_2}^- = R_2 J_{L_2}^+ \qquad R_2 = 1 - a_2 - t_2$$

where g_{th} is the threshold gain:

$$g_{th} = (-1/2L_2)\ln(R_1R_2) \quad (25)$$

J^+, J^- are the light intensity in the forward $+y$ and $-y$ directions, respectively; R_i, a_i and $t_i (i = 1, 2)$ are the reflectivity, absorption and transmission coefficients of mirrors at $y = 0$ and L_2, respectively.

Integrating equation (23) with respect to y and defining

$$I = \frac{1}{L_2}\int_0^{L_2} J\,dy$$

one obtains

$$g_{th}I = \frac{1}{L_2}\int_0^{L_2}\frac{1}{c}(B_{21}N_2 - B_{12}N_1)g(\nu)J\,dy$$

$$= \frac{1}{L_2}(J_{L_2}^+ - J_0^+ + J_0^- - J_{L_2}^-). \quad (26)$$

From equations (24) to (26), we can obtain J_0^- and $J_{L_2}^+$. Then the laser output power is

$$P_{laser} = A(J_0^- t_1 + J_{L_2}^+ t_2)$$

$$= A\frac{(t_2\sqrt{R_1} + t_1\sqrt{R_2})J_s}{(\sqrt{R_1} + \sqrt{R_2})(1 - \sqrt{R_1R_2})}(g_0L_2 + \ln\sqrt{R_1R_2}) \quad (27)$$

where A is the area of the output beam. It is shown that the output power is proportional to the product of saturation intensity J_s and small signal gain g_0.

3. Computational and numerical processes

3.1. Experimental apparatus

The numerical model described above has been used to simulate a high-pressure sealed CW TE CO_2 laser [10, 12].

Since the detailed configuration of this laser system has been reported previously [12, 13] only a brief review is given here. Figure 3 shows the glow discharge region schematically. The electrode configuration consists of 125 pin cathodes which are set in a row with equal spacings of 8 mm and a stainless steel, water-cooled planar anode. The length of the active medium

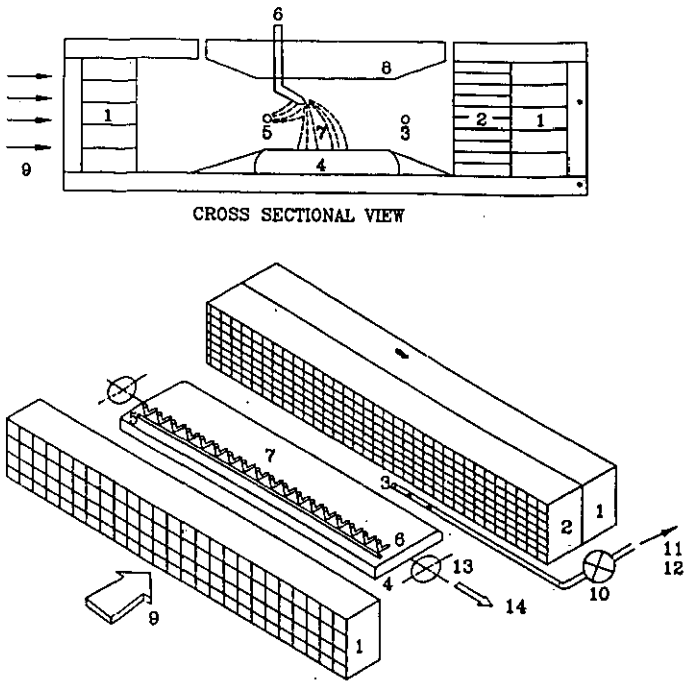

Figure 3. Schematic diagram of a sealed TE CO_2 laser with a gas analyser used in the present work. 1, Guided vane device; 2, ceramic monoliths; 3, gas sampling probe; 4, anode; 5, auxiliary electrode; 6, cathode; 7, glow discharge region; 8, insulator plate; 9, gas flow; 10, UHV leak valve; 11, mass analyser system; 12, turbomolecular pump system; 13, optical cavity; 14, laser output.

is about 100 cm. A DC power supply is used to provide a discharge current up to 5 A. The discharge voltage for the pressure range from 80 to 120 Torr is about to 2.4 kV (at a gas velocity of 25 m s^{-1}) and the cathode fall voltage is taken as 300 V [14]. Two axial blowers are used to circulate the gas mixture through the discharge region at a velocity range from 15 to 25 m s^{-1}. The temperature of the gas mixture entering the discharge region is kept at a constant temperature of 300 °K. Measurement conditions are made in CO_2:CO:N_2:He = 7:4:25:85 over a total pressure range of 80 to 120 Torr. The stable resonator consists of a Si total reflector with a radius of curvature of 5 m and a planar ZnSe partial reflector with 20% transmission.

3.2. Consideration of electrical-pumping and collision rate parameters

The spatial distribution of the electrical pumping term W_i depends on the electron density distribution. The pumping term W_i is defined as [9]

$$W_i(x) = N_e(x)N_i(x)X_i \quad (28)$$

where $N_e(x)$ is the electron density distribution along the x direction, $N_i(x)$ is the ith particle population density and X_i is the electron excitation rate with the ith particle.

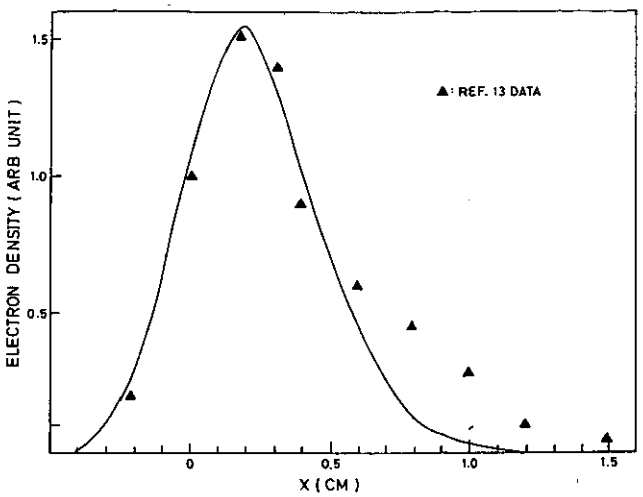

Figure 4. Electron density distribution along the flow direction at a total pressure of 99 Torr. The operational conditions and experimental points are extracted from [15]. The full curve is expressed by equation (29).

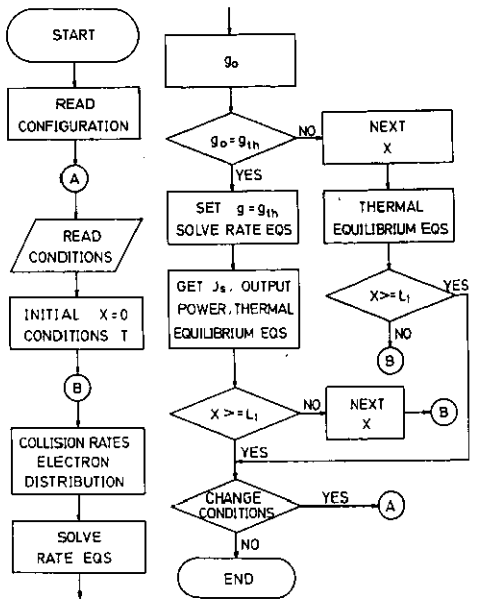

Figure 5. Numerical flow chart used to calculate the laser kinetic and discharge properties.

The spatial distribution of electron density N_e for the laser system has been measured by Ueguri and Lomura [15] and is shown in figure 4. Fitting the curve, an approximate expression of $N_e(x)$ can be written as [14]

$$N_e(x) = \left(\frac{Jc}{eV_d}\right) n_e(x) \tag{29}$$

where

$$n_e(x) = C \exp\left(-\frac{(x - x_0)^2}{2\beta^2}\right) \exp(\xi^2) \tag{30}$$

and

$$\xi \equiv \frac{1}{2}\left(\frac{1}{\tau_e} - \frac{x - x_0}{\beta}\right) \tag{31}$$

where V_d is the electron drift velocity, $V_d = 4.4 \times 10^6$ cm s^{-1} for $E/N \simeq 1.7 \times 10^{-16}$ V cm^2; $n_e(x)$ is the normalized electron distribution function; C is the normalized constant; τ_e is the decay constant of the electron density distribution, $\tau_e \simeq 2.5$; x_0 is the apparent displacement of the peak position due to the gas flow, $x_0 = 0.25$ cm at a gas flow velocity 25 m s^{-1}; and β is the half width of the distribution when the gas flow velocity is zero, $\beta = 0.15$ cm.

The electron–molecule excitation rates X_i are given in the literature [9, 16, 17]. We have used the values $X_1 = 4 \times 10^{-9}$ cm^3 s^{-1}, $X_2 = 4 \times 10^{-9}$ cm^3 s^{-1}, $X_3 = 5 \times 10^{-9}$ cm^3 s^{-1}, and $X_4 = 2 \times 10^{-8}$ cm^3 s^{-1}.

The collision rate constants for coupling of levels i and j by vibration–vibration (V-V) or vibration–translation (V-T) energy transfer processes are defined as $k_{ij} = \Sigma_m k_{ij}^m N_m$. Here k_{ij}^m is the rate constant for the appropriate (V-V) or (V-T) process that couples given levels i and j and involves collisions with a given molecule m present in the gas mixture in a number density N_m. The temperature dependence of k_{ij}^m can be obtained from [9].

3.3. Computer procedure and numerical flow chart

A flow chart for the computation of laser and gas discharge properties is shown in figure 5 and is explained as follows. The total pressure, gas mixture ratio, discharge region, mirror reflectivities R_1 and R_2, gas flow velocity, excitation conditions and the initial gas temperature are given. The initial position $x = 0$ is chosen from the top of the cathode pin. Then the electron density distribution $N_e(x)$, collision rates $k_{ij}(T)$ and the ith group particle population density $N_{i,x}^{\prime 0}$ can be calculated. The Runge–Kutta method has been used to obtain the population density $N_{i,x+d}^{\prime 0}$. Then the average population density $N_i^{\prime 0}$ between x and $x + d$ can be obtained from equations (3) by using the Gauss direct elimination method. When N_2^0 and N_1^0 are obtained, the small signal gain g_0 can be calculated from equation (18). If g_0 is greater than the threshold gain g_{th}, then the laser output power from this small region can be derived from equation (27). The saturation intensity J_s can be calculated from equation (22). The new working parameters such as the gas temperature T, pressure p, flow velocity u, and gas density ρ for the next small region, are obtained from the thermodynamic equations (14a) to (14d). With $N_{i,x+d}^{\prime}$ and these new working parameters as the initial conditions, we can calculate the population inversion, small signal gain, saturation intensity and laser output power in the next thin layer and the program repeats the cycle sequentially. Therefore, by using this program the spatial distribution of small signal gain, saturation intensity, and laser output along the gas flow

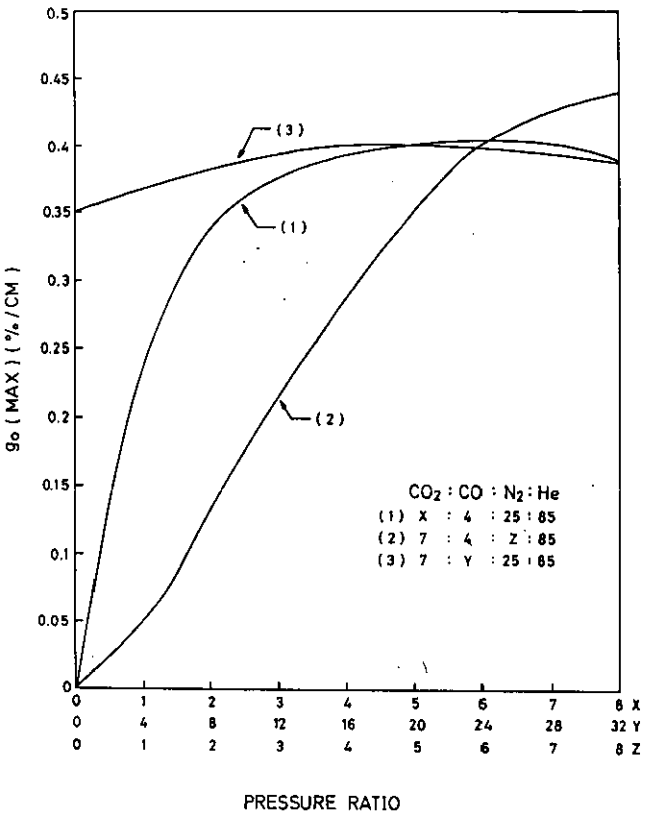

Figure 6. Variation of maximum small signal gain with various pressure ratios. Total pressure = 100 Torr, gas velocity = 25 m s^{-1}, and discharge current = 2 A.

direction and the total output power under different discharge and gas conditions, can be determined.

4. Results and discussion

4.1. The influence of gas mixture

A small increment d of 0.5 mm is chosen throughout this theoretical calculation. In order to obtain the optimum ratio of gas mixture, the small signal gains versus the partial pressures of each of the individual gases in the mixture have been calculated.

Figure 6 shows a plot of the maximum small signal gain $g_{0(max)}$ as a function of CO_2, CO, and N_2 gases. Let the ratio of gas mixture be $CO_2:CO:N_2:He = x:4:25:85$. When x increases from 1 to 9, we find that the small signal gain increases steadily up to a broad maximum and subsequently decreases upon further increases in CO_2 concentration.

A somewhat similar behaviour is obtained when the CO concentration is varied from $y = 0$ to $y = 8$ in the gas mixture of $CO_2:CO:N_2:He = 7:y:25:85$. $g_{0(max)}$ for CO is found to occur near $y = 4$ to 6. A small amount of CO gas is effective for excitation to the upper laser level and deactivation of the lower laser level [7]. However, further increase of CO concentration would cause net collisional deactivation of the upper laser level of CO_2 molecules [13]. In fact, the main purpose of the addition of CO in TE CO_2 laser systems is to improve the long-term discharge stability under the sealed-off operation [12–14].

Let the ratio of the gas mixture be $CO_2:CO:N_2:He = 7:4:z:85$. When z changes from 1 to 32, the gain increases monotonically because the energy transfer between the levels of $CO_2(001)$ and $N_2(v = 1)$ increases. However, a further addition of N_2 would cause the glow discharge to transit to an unstable discharge for a practical operation. Therefore, there also exists an optimum value of N_2 concentration.

In summary, a gas composition of $CO_2:CO:N_2:He = 7:4:25:85$ has been chosen for our laser system under the consideration of both high small signal gain and stable discharge.

4.2. The influence of total pressure

The spatial distribution of g_0 along the gas flow direction at different total pressures p is shown in figure 7(a). It is shown that the small signal gain increases rapidly to reach a maximum value and then decreases slowly. The maximum gain is lower for a relatively high pressure. The position of the peak gain occurs near $x = 0.7$ cm and shifts to downstream slightly for a lower pressure case. The decay rate after the peak gain at higher pressure is faster than that at lower pressure. The distribution of g_0 along the gas flow is relatively non-uniform. This is a result of the combined influences of the discharge non-uniformity and the dynamics of molecular excitation and relaxation processes in the fast flow of gas.

Since the width of gain distribution varies with the total pressure due to the existence of gas flow, it is reasonable that we deal with the dependence on pressure p of the average quantity $\overline{g_0} = (1/L)\int_0^L g_0(x)\,dx$ rather than the maximum value of $g_0(x)$, where L is the distance which the small signal gain decays to zero. Referring to figure 8, it is found that $\overline{g_0}$ is approximately proportional to p^{-1}. This relation can be explained from the fact that the pumping rates A_i, the relaxation rates k_{ij} and the collision-broadened linewidth $\Delta\nu$ are proportional to the total pressure for the high-pressure laser system and g_0 is proportional to $(\Delta\nu)^{-1}$. The gain distribution $g_0(x)$ under the operational conditions of Akiba *et al* [14] is also plotted in figure 7(a).

The spatial distribution of saturation intensity J_s along the gas flow direction is shown in figure 7(b). It demonstrates that J_s increases slightly along the flow direction. However, the average quantity $\overline{J_s} = (1/L)\int_0^L J_s(x)\,dx$ has a nearly quadratic dependence on the total pressure as shown in figure 8. This relation can be explained by the expression in the appendix (equation (A.18)) where both k_{ij} and $\Delta\nu$ are proportional to p.

The output power distribution is shown in figure 7(c) and the total output power against total pressure which shown in figure 9 is the integration of the output power distribution from 0.2 to 2.0 cm along the gas

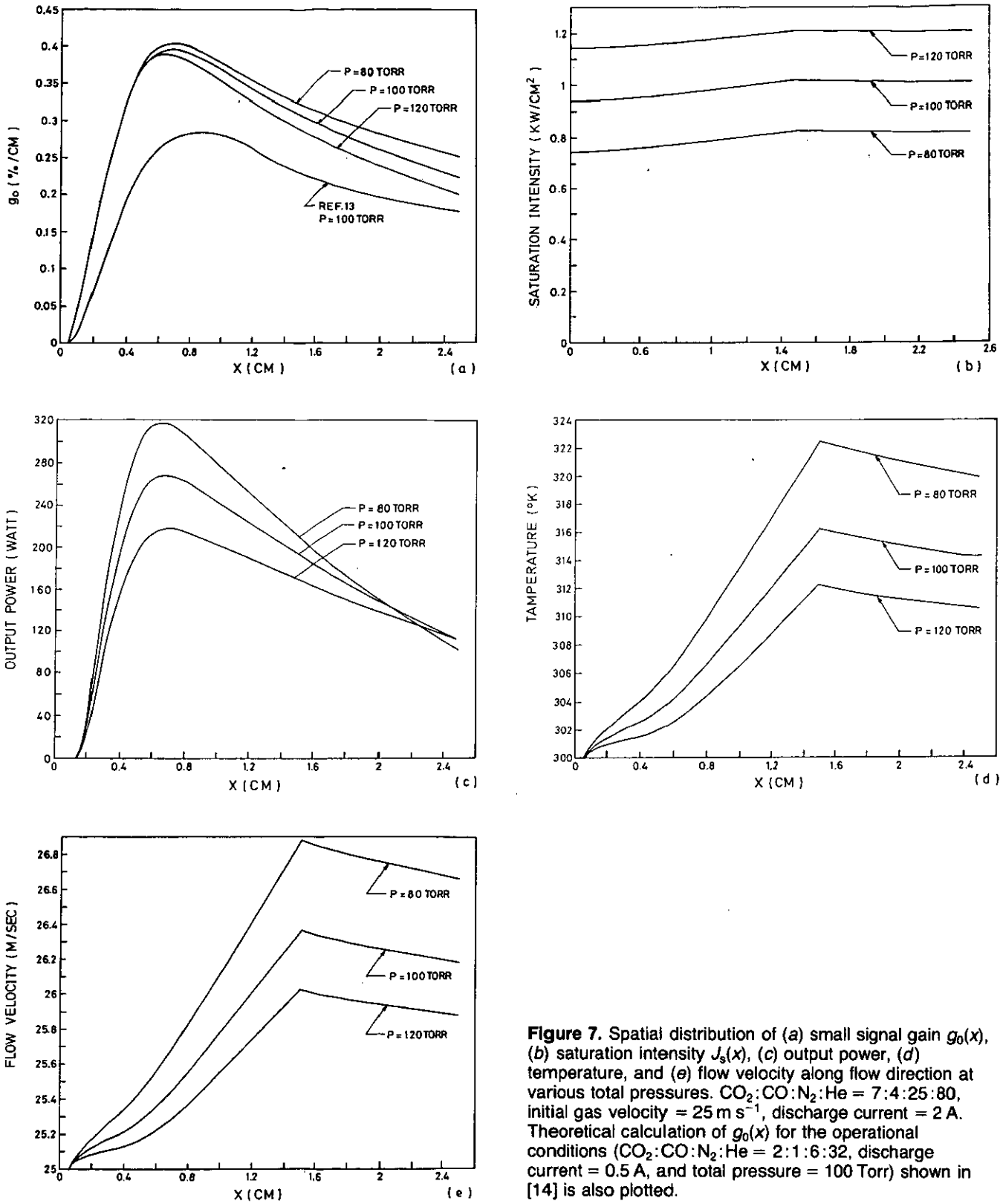

Figure 7. Spatial distribution of (*a*) small signal gain $g_0(x)$, (*b*) saturation intensity $J_s(x)$, (*c*) output power, (*d*) temperature, and (*e*) flow velocity along flow direction at various total pressures. CO_2:CO:N_2:He = 7:4:25:80, initial gas velocity = 25 m s^{-1}, discharge current = 2 A. Theoretical calculation of $g_0(x)$ for the operational conditions (CO_2:CO:N_2:He = 2:1:6:32, discharge current = 0.5 A, and total pressure = 100 Torr) shown in [14] is also plotted.

flow direction and with a discharge gap of 1.7 cm. Since the laser output power is proportional to the product of the small signal gain and saturation intensity, it is proportional to the total pressure.

The variations of temperature and flow velocity along the gas flow direction for several values of total pressure are shown in figure 7(*d*) and (*e*) respectively, and can be explained by the thermodynamic equations (11) to (13).

4.3. The influence of gas flow velocity

The small signal gain g_0 distribution along the gas flow direction is plotted in figure 10 at various flow velocit-

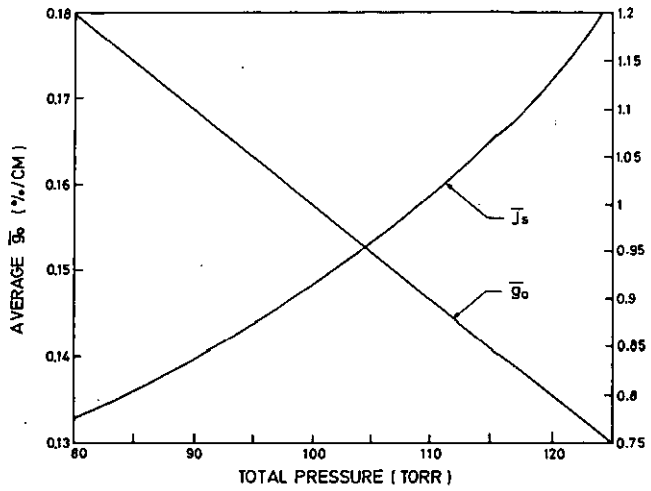

Figure 8. The dependence of average gain $\overline{g_0} = (1/L) \int_0^L g_0(x)\,dx$ and average saturation intensity $\overline{J_s} = (1/L) \int_0^L J_s(x)\,dx$ on total pressure. (Same operational conditions as shown in figure 7.)

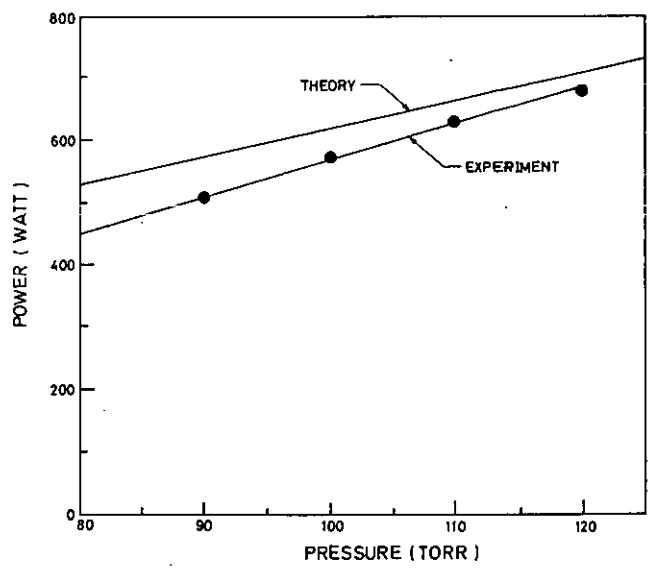

Figure 9. The dependence of total output power on total pressure. (Same operational conditions as shown in figure 7.)

ies. The variation of gain with velocity indicates that the major effect of the flow on this system is to reduce the peak gain slightly and to spread it out downstream [18]. Figure 11 shows the flow velocity dependence of $(1/L) \int_0^L g_0(x)\,dx$; it is found that the average gain increases slightly with increasing the flow velocity. On the other hand, the average saturation intensity $(1/L) \int_0^L J_s(x)\,dx$ is found to be relatively sensitive to gas flow variations. Figure 11 shows that $(1/L) \int_0^L J_s(x)\,dx$ is almost proportional to the gas flow velocity. The total output power against flow velocity is plotted in figure 12. The experimental results are also shown. Compared to the experimental results, when the gas flow velocity is changed from 19 m s^{-1} to 25 m s^{-1}, good agreement between theory and experiment is obtained. However, when the flow velocity is below 17 m s^{-1}, the uniform glow discharge changes to an unstable discharge and the total output power drops abruptly in practical operation. Therefore, a higher flow velocity is not only favourable in the laser output power but also for stable discharges [19].

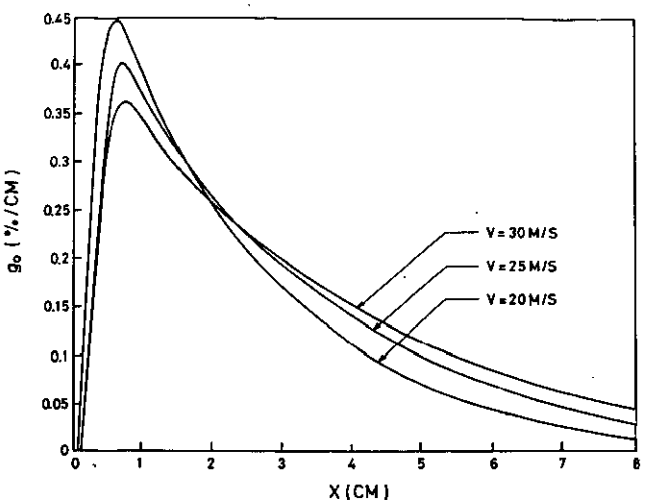

Figure 10. Small signal distribution along flow direction at various flow velocities CO_2:CO:N_2:He = 7:4:25:85, total pressure = 100 Torr, discharge current = 2 A.

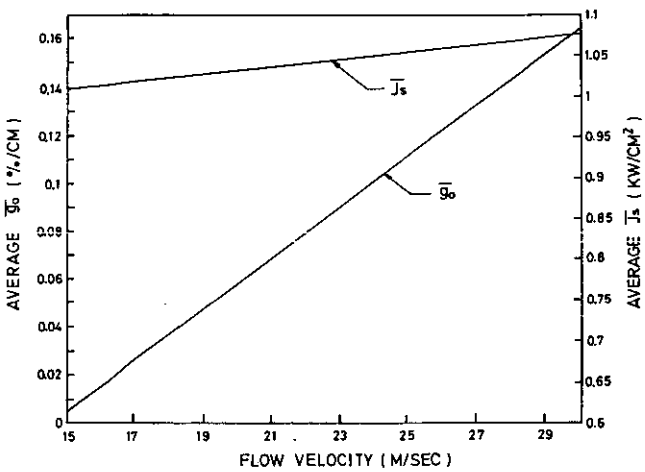

Figure 11. The dependence of average gain and average saturation intensity on gas flow velocity. (Same operational conditions as shown in Fig. 10.)

4.4. The influence of discharge current

The spatial distribution of g_0 at different discharge currents and the dependence of average gain on discharge current are shown in figures 13 and 14, respectively. It is shown that the average gain is proportional to the discharge current. This may be explained by the fact that the electrical-pumping term W_i increases linearly with increasing discharge current and the small signal gain is proportional to the electrical-pumping term. Figure 15 shows the total output power against discharge current; the experimental results are also

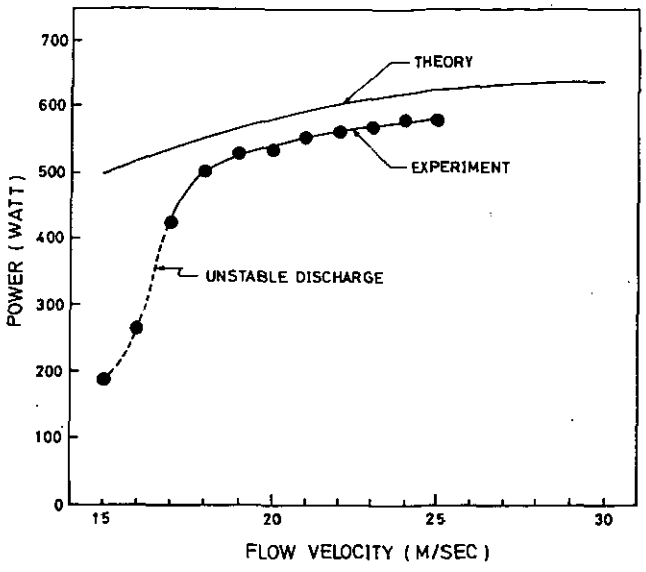

Figure 12. The dependence of total output power on gas flow velocity. (Same operational conditions as shown in figure 10.)

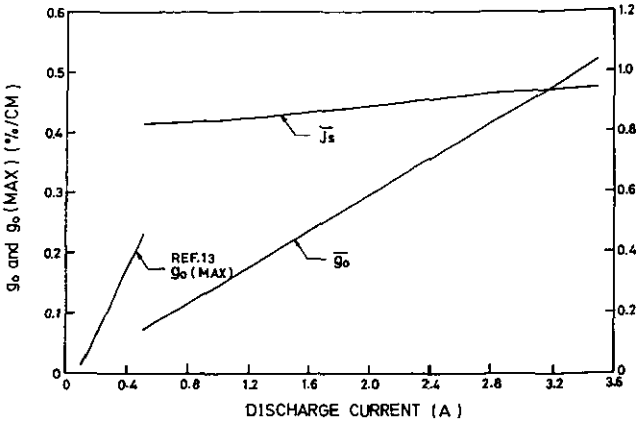

Figure 14. The dependence of average gain and saturation intensity on discharge current. (Same operational conditions as shown in figure 13.) Theoretical calculation of the dependence of $g_{0(max)}$ on discharge current for the operational conditions shown in [14] is also plotted.

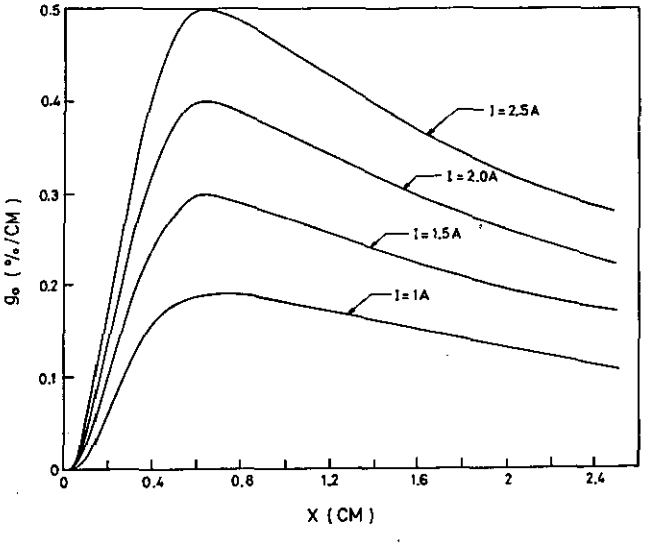

Figure 13. Small signal gain distribution along flow direction at various discharge currents. CO_2:CO:N_2:He = 7:4:25:85, total pressure = 100 Torr, gas flow velocity = 25 m s^{-1}.

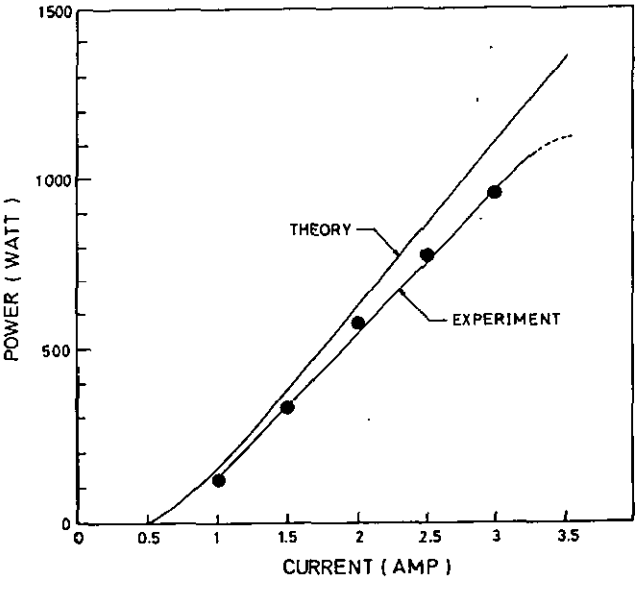

Figure 15. The dependence of total output power on discharge current under the same gas conditions as shown in figure 13.

shown. When the discharge current is 3.5 A, the glow discharge tends to arc and the output power fluctuates tremendously.

5. Conclusion

A numerical model and the important energy transfer processes involved have been described in detail to develop the theoretical model of a TE CW CO_2 laser. A simplified numerical process is adapted to carry out the calculation. The spatial distribution of small signal gain and saturation intensity and the total output power are presented as functions of gas composition, total pressure, gas flow velocity and discharge current. There are some valuable results and suggestions from this numerical analysis.

(1) The choice of the optimum gas composition for TE CO_2 lasers should consider both factors of high gain and stable discharge. The gas mixture of CO_2:CO:N_2:He = 7:4:25:85 is the optimum composition for our laser system examined here.

(2) The small signal gain and the saturation intensity are approximately proportional to p^{-1} and p^2, respectively, at high-pressure operation where p is the

total pressure about 100 Torr. Therefore, the total output power is proportional to p [13].

(3) The higher flow velocity reduces the peak gain slightly and spreads it out downstream. The saturation intensity, however, increases linearly and thus the total output power also increases almost linearly as the flow velocity increases. It is suggested that either an unstable resonator or a multipass folded cavity may be used to extract the power efficiently.

(4) A higher gas flow velocity is more favourable for discharge stability.

(5) The position of the maximum gain $g_{0(\max)}$ will shift at different flow velocities or pressures. Therefore, the optical axis of the cavity should be readjusted when the operational conditions change.

(6) The small signal gain increases linearly with increasing the discharge current. The total output power is directly proportional to the discharge current.

The theoretical results from this model are in good agreement with the experimental data of our laser system and the results of Akiba *et al* [14], confirming the usefulness of the model and understanding of the CW TE laser performances.

Acknowledgment

This work was supported by the National Science Council of the Republic of China, project no NSC78-0417-E009-01.

Appendix

In order to simplify the analytical solutions we may not consider the collision rates r_{34} and k_{43} in equations (5).

$$A_1 - (k_{10} + k_f)N_1 + (B_{21}N_2 - B_{12}N_1)g(\nu)\frac{J}{ch\nu} + k_f N_1^0 = 0 \tag{A.1}$$

$$A_2 - (k_{21} + k_{23} + k_{24} + k_f)N_2 + (B_{21}N_2 - B_{12}N_1)g(\nu)\frac{J}{ch\nu} + k_{32}N_3 + k_{42}N_4 + k_f N_2^0 = 0 \tag{A.2}$$

$$A_3 + k_{23}N_2 - (k_{32} + k_f)N_3 + k_f N_3^0 = 0 \tag{A.3}$$

$$A_4 + k_{24}N_2 - (k_{42} + k_f)N_4 + k_f N_4^0 = 0. \tag{A.4}$$

From equations (A.2) to (A.4) we have

$$(A_2 + A_3 + A_4) - (k_{21} + k_f)N_2 - (B_{21}N_2 - B_{12}N_1)g(\nu)\frac{J}{ch\nu} - k_f N_3 - k_f N_4 + k_f(N_2^0 + N_3^0 + N_4^0) = 0. \tag{A.5}$$

For $J = 0$, from equations (A.1), (A.5), (A.3), and (A.4) we obtain

$$N_1^0 = \frac{A_1}{k_{10}} \tag{A.6}$$

$$N_2^0 = \frac{A_2 + A_3 + A_4}{k_{21}} \tag{A.7}$$

$$N_3^0 = \frac{A_3}{k_{32}} + \frac{k_{23}}{k_{32}}\frac{A_2 + A_3 + A_4}{k_{21}} \tag{A.8}$$

$$N_4^0 = \frac{A_4}{k_{42}} + \frac{k_{24}}{k_{42}}\frac{A_2 + A_3 + A_4}{k_{21}}. \tag{A.9}$$

From (A.3) and (A.4) we obtain

$$N_3 = \frac{A_3 + k_{23}N_2 + k_f N_3^0}{k_{32} + k_f} \tag{A.10}$$

$$N_4 = \frac{A_4 + k_f N_4^0 + k_{24}N_2}{k_{42} + k_f}. \tag{A.11}$$

Substituting (A.10) and (A.11) into (A.5) and rearranging yields

$$R_2 - \frac{N_2}{t_2} - (B_{21}N_2 - B_{12}N_1)g(\nu)\frac{J}{ch\nu} = 0 \tag{A.12}$$

where

$$R_2 = (A_2 + A_3 + A_4)(k_f + 1) - k_f\left(\frac{A_3 + k_f N_3^0}{k_{32} + k_f} + \frac{A_4 + k_f N_4^0}{k_{42} + k_f}\right)$$

$$t_2 \equiv \left(k_{21} + k_f + \frac{k_f k_{23}}{k_f + k_{32}} + \frac{k_f k_{24}}{k_f + k_{42}}\right)^{-1}.$$

Similarity, equation (A.1) can be rewritten as

$$R_1 + \frac{N_1}{t_1} - (B_{21}N_2 - B_{12}N_1)g(\nu)\frac{J}{ch\nu} = 0 \tag{A.13}$$

where $R_1 \equiv A_1 + k_f N_1^0$

$$t_1 \equiv (k_{10} + k_f)^{-1}.$$

The small signal gain g_0. Solving (A.12) and (A.13) for $J = 0$, we can obtain $N_1^0 = R_1 t_1$ and $N_2^0 = R_2 t_2$. The unsaturated gain then becomes

$$g_0 = \frac{1}{c}(B_{21}N_2^0 - B_{12}N_1^0)g(\nu) = \frac{1}{c}\left(B_{21}\frac{A_2 + A_3 + A_4}{k_{21}} - B_{12}\frac{A_1}{k_{10}}\right)g(\nu) \tag{A.14}$$

The saturation intensity J_s. From (A.12) and (A.13) we have

$$N_1 = \frac{R_2 B_{21}(J/ch\nu) + R_1(t_2^{-1} + B_{21}(J/ch\nu))}{1 + (B_{21}t_2 + B_{12}t_1)(J/ch\nu)}t_1 t_2 \tag{A.15}$$

$$N_2 = \frac{R_1 B_{12}(J/ch\nu) + R_2(t_1^{-1} + B_{12}(J/ch\nu))}{1 + (B_{21}t_2 + B_{12}t_1)(J/ch\nu)} t_1 t_2. \tag{A.16}$$

Then the saturated gain becomes

$$g = \frac{1}{c}(B_{21}N_2 - B_{12}N_1)g(\nu)$$

$$= \frac{1}{c}\frac{(B_{21}R_2t_2 - B_{12}R_1t_1)g(\nu)}{1 + (J/ch\nu)(B_{12}t_1 + B_{21}t_2)g(\nu)}$$

$$= \frac{1}{c}\frac{g_0}{1 + (J/J_s)} \tag{A.17}$$

where $J_s = ch\nu[(B_{12}t_1 + B_{21}t_2)g(\nu)]^{-1}$

$$= ch\nu\left(\frac{B_{12}}{k_{10}+k_f} + \frac{B_{21}(k_{32}+k_f)(k_{42}+k_f)}{(k_{21}+k_f)(k_{32}+k_f)(k_{42}+k_f) + k_{23} + k_f(k_{42}+k_f) + k_{24} + k_f(k_{32}+k_f)}\right)^{-1}\frac{1}{g(\nu)} \tag{A.18}$$

From homogeneous broadening we obtain

$$J_s = ch\nu\frac{\pi\Delta\nu}{2B_{21}}\left(\frac{g_2/g_1}{k_{10}+k_f} + \frac{(k_{32}+k_f)(k_{42}+k_f)}{(k_{21}+k_f)(k_{32}+k_f)(k_{42}+k_f) + k_{23} + k_f(k_{42}+k_f) + k_{24} + k_f(k_{32}+k_f)}\right)^{-1} \tag{A.19}$$

and for the case of $k_f \gg k_{ij}$,

$$J_s = ch\nu\left(\frac{B_{12}}{k_f} + \frac{B_{21}k_f^2}{k_f^3}\right)^{-1} = ch\nu\frac{k_f}{B_{12}+B_{21}}. \tag{A.20}$$

References

[1] Cool T A 1969 Power and gain characteristics of high speed flow lasers *J. Appl. Phys.* **40** 3563

[2] Tulip J and Seguin H 1971 Gas-dynamic CO_2 laser pumped by combustion of hydrocarbons *J. Appl. Phys.* **42** 3393

[3] Goela J S, Healy J J and Morse T F 1975 Inhomogeneous broadening and rotational relaxation effects in a molecular gas flow laser *J. AIAA* **13** 1629

[4] Anderson J D 1970 Time-dependent analysis of population inversions in an expanding gas *Phys. Fluids* **13** 1983

[5] Yoder M J, Legner H H, Jacob J H and Ahouse D R 1978 Theoretical and experimental performance of a high-power CW electron-beam-sustained electric laser *J. Appl. Phys.* **49** 3171

[6] Armandillo E and Kay A S 1980 Modelling of transverse-flow CW CO_2 lasers: theory and experiment *J. Phys. D: Appl. Phys.* **13** 321

[7] Wittman W J 1987 *The CO_2 Laser* (Berlin: Springer)

[8] DeMaria A J 1973 High power CO_2 lasers *Proc. IEEE* **61** 731

[9] Smith K and Thompson R M 1978 *Computer Modelling of Gas Lasers* (New York: Plenum)

[10] Wu K-H 1989 Sealed CW transversely-excited CO_2 laser operated with active catalysts *Appl. Phys. Lett.* **55** 2689

[11] Verdeyen J V 1981 *Laser Electronics* (Englewood Cliffs, NJ: Prentice-Hall)

[12] Wu K-H 1990 Investigation of a long-term sealed CW transversely-excited CO_2 laser *J. Chin. Inst. Eng.* **13** 471

[13] Nagai H, Hishi M, Shibayama, Nagai A and Akiba T 1982 High-pressure sealed CW CO_2 laser with high efficiency *IEEE J. Quant. Electron.* **18** 416

[14] Akiba T, Nagai H and Hishii M 1979 Gain characteristics of an atmospheric sealed CW CO_2 laser *IEEE J. Quant. Electron.* **15** 162

[15] Ueguri S and Komura H 1975 Electron density distributions in glow discharge under a gas-flow condition *Hoden Kenkyu* **61** 52 (in Japanese)

[16] Nighan W L and Bennet J H 1969 Electron energy distribution functions and vibrational excitation rates in CO_2 laser mixtures *Appl. Phys. Lett.* **14** 240

[17] Manes K R and Segiun H J 1972 Analysis of the CO_2 TEA laser *J. Appl. Phys.* **43** 5073

[18] Seguin H J and Sedgwick G 1972 Low voltage gas transport TE CO_2 laser *Appl. Opt.* **11** 745

[19] Shwartz J and Wasserstrom E 1975 The role of gas flow and turbulence in electric discharge lasers *Isr. J. Technol.* **13** 122